Incorporating the Effects of 3D Radiative Transfer in the Presence of Clouds into Two-Stream Multilayer Radiation Schemes

ROBIN J. HOGAN AND JONATHAN K. P. SHONK

Department of Meteorology, University of Reading, Reading, United Kingdom

ABSTRACT

This paper presents a new method for representing the important effects of horizontal radiation transport through cloud sides in two-stream radiation schemes. Ordinarily, the radiative transfer equations are discretized separately for the clear and cloudy regions within each model level, but here terms are introduced that represent the exchange of radiation laterally between regions and the resulting coupled equations are solved for each layer. This approach may be taken with both the direct incoming shortwave radiation, which is governed by Beer's law, and the diffuse shortwave and longwave radiation, governed by the two-stream equations. The rate of lateral exchange is determined by the area of cloud "edge." The validity of the method is demonstrated by comparing with rigorous 3D radiative transfer calculations in the literature for two cloud types in which the 3D effect is strong, specifically cumulus and aircraft contrails. The 3D effect on shortwave cloud radiative forcing varies between around -25% and around $+100\%$, depending on solar zenith angle. Even with an otherwise very simplistic representation of the cloud, the new scheme exhibits good agreement with the rigorous calculations in the shortwave, opening the way for efficient yet accurate representation of this important effect in climate models.

1. Introduction

Clouds are a key component of the climate system on account of their strong interaction with radiation (Randall et al. 2007). Numerous studies have highlighted the radiative flux bias in climate models resulting from neglect of subgrid cloud inhomogeneity (e.g., Cahalan et al. 1994; Barker et al. 1999; Pomroy and Illingworth 2000). Several methods to represent subgrid inhomogeneity have been proposed that are efficient enough to be included in climate models (Barker 1996; Pincus et al. 2003; Shonk and Hogan 2008). Some studies have examined cloud structure in observational data (Oreopoulos and Cahalan 2005), while others have quantified the impact of cloud horizontal structure and vertical overlap on the global radiation budget using reanalysis data (Shonk and Hogan 2010) and model simulation (Morcrette and Jakob 2000; Pincus et al. 2006; Shonk et al. 2012).

A related piece of missing physics in the treatment of clouds and radiation in climate models is transport of radiation through cloud sides. In current climate models, radiation is allowed to enter or leave a cloud in a model level only through its base or top. Full 3D radiative transfer calculations have demonstrated that this can lead to substantial errors in cloud radiative forcing, particularly for cumulus clouds (e.g., Pincus et al. 2005), deep convection (DiGiuseppe and Tompkins 2003), aircraft contrails (Gounou and Hogan 2007), and cirrus uncinus (Zhong et al. 2008). The magnitude of the 3D effect (the difference in radiative fluxes between radiation calculations including and neglecting 3D transport) is dependent on the ratio of the area of cloud side to the total cloud cover. Therefore, cumulus clouds are of particular importance when considering 3D radiative effects: although when present they have a cloud cover of only around 0.25, cumulus regimes cover huge stretches of the tropical oceans.

The myriad of ways that radiation can interact with a complex cloud field makes it very difficult to devise an accurate way to represent 3D effects that is efficient enough to use in a general circulation model (GCM). Therefore, despite the numerous detailed studies on individual cloud fields, no global-scale calculations have

Corresponding author address: Robin Hogan, Department of Meteorology, University of Reading, Earley Gate, P.O. Box 243, Reading RG6 6BB, United Kingdom.
E-mail: r.j.hogan@reading.ac.uk

been performed to estimate the impact of 3D effects on the radiation budget in both the shortwave and longwave and the possible feedback on cloud properties and other atmospheric variables. It is sometimes suggested that 3D effects must be quite modest on a global scale, but we cannot assume this until a scheme to represent 3D effects comprehensively in a radiation scheme is applied in a GCM and climate simulations are performed.

One approach is to apply stochastic theory to the radiative transfer problem by defining probability density functions that determine whether a photon is in cloud or clear sky (Titov 1990). Photon transport through cloud sides can then be represented by adding two extra terms to the basic radiative transfer equations weighted by the probability density function of the photon arriving at a cloud boundary (Malvagi et al. 1993). A 3D stochastic radiative transfer code was described and tested by Lane-Veron and Somerville (2004). While its results were promising, it was found to be inappropriate for certain cloud scenarios and has yet to be implemented in a GCM. Another approach was used by Várnai and Davies (1999) to show the radiative effects of allowing radiative transfer through cloud sides. Their tilted independent column approximation (TICA) calculated fluxes along profiles of cloud aligned with the direction of the sun, therefore allowing direct radiation to pass between cloud and clear-sky regions. Unfortunately, the expense of an ICA-type calculation makes this approach much too expensive for GCM use.

The only method that has been implemented in a GCM to date is the so-called exponential–solar zenith angle–random (EXP-SZA-RAN) approach of Tompkins and DiGiuseppe (2007), which makes the overlap of clouds in different layers more random with increasing solar zenith angle. The resulting increase in total cloud cover is intended to approximately represent the fact that when the sun is near the horizon, incoming solar radiation is more likely to intercept a cloud than when it is overhead. When included in a GCM, they found local changes in top-of-atmosphere net shortwave flux of up to 200 W m^{-2}. Although this method has the advantage of being conceptually simple and easy to implement in existing radiation schemes, it has several shortcomings. Firstly, it only treats 3D effects associated with direct incoming shortwave radiation, not the effects associated with diffuse transport of shortwave and longwave radiation, which are not dependent on solar zenith angle. It was shown by Heidinger and Cox (1996) that there is a significant 3D longwave effect for cumulus clouds, and in the next section it will be shown that diffuse transport of shortwave radiation is also important via a mechanism we refer to as shortwave side escape.

In this paper we present a new method for representing the interaction of radiation with clouds in GCMs that is able to overcome these difficulties. It uses the familiar division of a model grid box into clear and cloudy regions, or in the case of the ''Triplecloud'' method of Shonk and Hogan (2008) a split into three regions: two cloudy and one clear. Extra terms are introduced into the equations of radiative transfer that represent the lateral exchange of radiation between regions.

In section 2, a conceptual model of 3D radiative transfer is presented that summarizes the effect of 3D transport by three mechanisms: two in the shortwave and one in both the shortwave and longwave. Results of shortwave 3D radiative transfer calculations from the literature are then presented, which are explained in terms of the first two effects. In sections 3 and 4 we describe how the various parts of a 1D radiative transfer calculation may be modified to include 3D effects. Then in section 5, a simple implementation of the new scheme is used to reproduce the results from the literature shown in section 2.

2. Conceptual model

To aid the formulation of the new radiative transfer scheme, it is necessary to present a conceptual model for the ways that 3D effects in the presence of clouds change net fluxes in the longwave and shortwave. This will then be used to explain qualitatively some full 3D radiative transfer calculations in the literature. Figure 1 presents what we consider to be the three dominant mechanisms of 3D radiative transport, adapted from Gounou and Hogan (2007). Várnai and Davies (1999) proposed a more complex model with four separate mechanisms for the shortwave alone, but for the purposes of this paper three mechanisms are sufficient.

The first mechanism—shortwave side illumination—is the most widely studied. It increases with solar zenith angle and results in a larger fraction of incoming solar radiation being reflected back to space than in the equivalent 1D calculation in which no horizontal transport between regions is permitted. The example in Fig. 1a shows a case when all of the incoming solar radiation intercepts a cloud, even though the cloud cover is only one-third. In the equivalent 1D calculation, two-thirds of the incoming radiation would reach the surface without intercepting the cloud (neglecting gaseous scattering and absorption for simplicity).

Figure 2 shows the percentage change to top-of-atmosphere (TOA) shortwave cloud radiative forcing, as a function of solar zenith angle, calculated using full 3D radiative transfer and reported in the literature for several different cloud types. Here, cloud radiative forcing
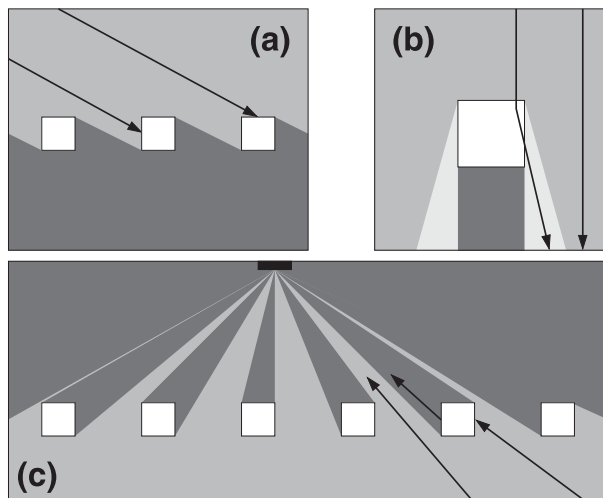
FIG. 1. Schematic explaining how 3D radiative transfer affects CRF, with the lighter colors outside clouds indicating more intense radiation and the darker colors less intense radiation. (a) Shortwave side illumination: at high solar zenith angles, a greater fraction of incoming solar radiation is intercepted by cloud than in standard 1D radiative transfer, increasing the CRF. (b) Shortwave side escape: at low solar zenith angles, the radiation that escapes out of cloud sides tends to be forward scattered toward the ground, decreasing the CRF. (c) Shortwave and longwave side exchange: above a field of clouds, the clouds subtend a greater fraction of the downward-looking hemisphere [accounting for $\cos(\theta)$ dependence of their contribution to the upwelling irradiance] than the areal cloud coverage. Hence, the longwave CRF is larger than in the ICA. In the shortwave, less reflected radiation from the surface is able to escape back to space.

(CRF) is defined as the difference between the clear-sky and cloudy-sky upwelling shortwave radiation at TOA; that is,

$$\mathrm{CRF} = F^+_{\mathrm{clear,TOA}} - F^+_{\mathrm{cloudy,TOA}}. \quad (1)$$

Thus, shortwave CRF is negative except over very reflective snow-covered surfaces. The quantity shown in Fig. 2 is given by $100 \times (\mathrm{CRF_{3D}} - \mathrm{CRF_{1D}})/\mathrm{CRF_{1D}}$, where $\mathrm{CRF_{3D}}$ is the CRF calculated using a full 3D radiative transfer model, while $\mathrm{CRF_{1D}}$ is the CRF calculated using a standard 1D radiative transfer model.

It can be seen in Fig. 2 that, for cumulus with a solar zenith angle greater than around 45°, the magnitude of the CRF is increased significantly because of the mechanism of shortwave side illumination. For solar zenith angles greater than around 80°, the calculations of Pincus et al. (2005) for cumulus clouds predict that the magnitude of CRF can be doubled. The results of Gounou and Hogan (2007) for aircraft contrails confirm that side illumination is responsible: when they orientated their contrails perpendicular to the sun (the solid gray line in Fig. 2), thereby maximizing the solar illumination of the
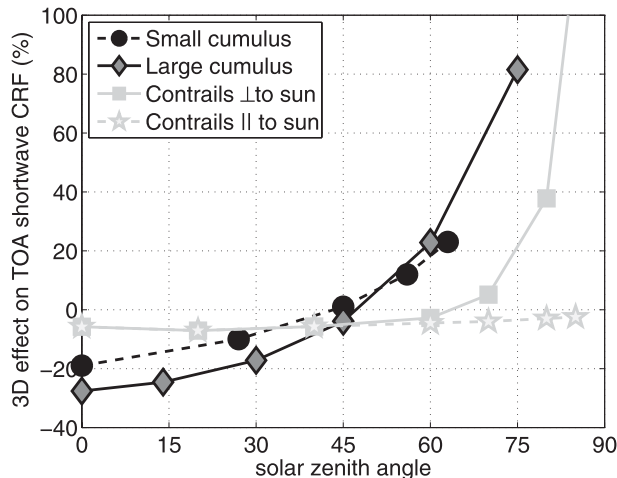

FIG. 2. The effect of 3D radiative transfer on shortwave TOA CRF, vs solar zenith angle, for cumulus clouds and contrails, calculated rigorously using full 3D radiative transfer codes. The "small cumulus" results are from Benner and Evans (2001) and the large cumulus from Pincus et al. (2005), both of whom used Monte Carlo models. The contrail results are from Gounou and Hogan (2007), who used the spherical harmonics discrete ordinate method (SHDOM) of Evans (1998).

side of the contrail, the 3D effect was maximized, but orientating their contrails parallel to the sun (the dashed gray line in Fig. 2), thereby removing any illumination of the side of the contrail, the CRF enhancement at high solar zenith angles was removed.

It is clear from Fig. 2 that side illumination is not the only shortwave 3D effect, since for solar zenith angles less than 45°, the magnitude of the CRF for cumulus and contrails is reduced when 3D transport is included, by up to 27% in the study of Pincus et al. (2005). This we explain in Fig. 1b by the mechanism of shortwave side escape, referred to as "downward escape" by Várnai and Davies (1999). Shortwave radiation from an overhead sun that enters a cloud through its top may escape from the sides of a cloud, where in a 1D calculation it may not and is more likely to be reflected back to space. Since cloud particles are typically larger than the wavelength of the radiation, the scattering is predominantly in the forward direction, and so radiation escaping from the side of a cloud is more likely to be directed toward the surface than back to space. Therefore, this mechanism reduces CRF relative to a 1D calculation.

In the longwave, inclusion of 3D transport tends to increase the CRF owing to the presence of cloud sides, making the cloud a more effective emitter and absorber, as illustrated in Fig. 1c and which we refer to as longwave side exchange. Essentially the same mechanism was identified by Killen and Ellingson (1994). It was estimated by Heidinger and Cox (1996) that 3D transport in cumulus
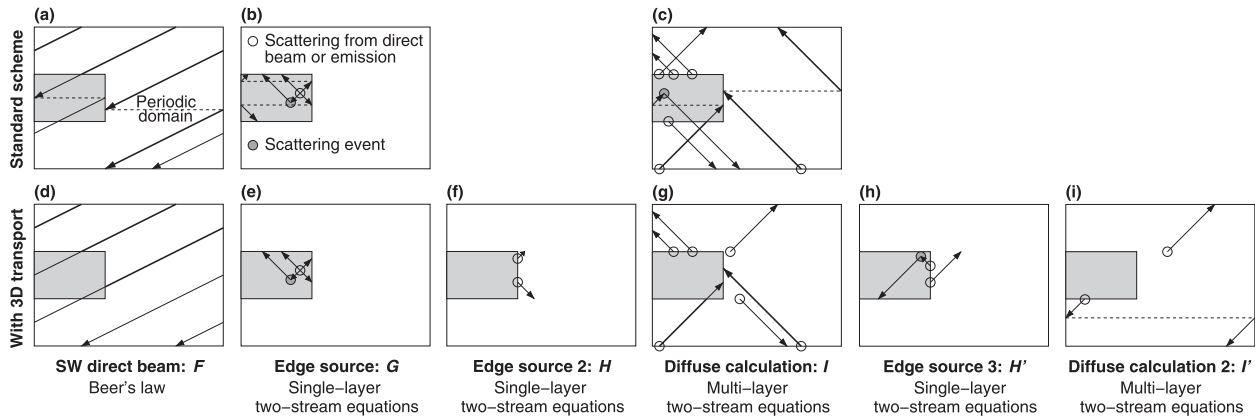
FIG. 3. Schematic showing the various steps in a 1D radiation scheme. (top) The three steps in a standard 1D scheme: (a) calculation of the penetration of the direct solar beam to various levels in the atmosphere, (b) the use of this to calculate the upwelling and downwelling radiation sources at layer edges, and (c) the use of surface and edge sources to calculate the profile of diffuse upwelling and downwelling fluxes. In each case, radiation within a particular region (clear or cloudy) is not permitted to travel laterally to the other region; rather, the regions are treated as periodic and the implicit transport from one side of a region to the other is illustrated by the dashed horizontal lines. (bottom) The equivalent steps in our new scheme, including three additional steps, as described in detail in section 3. The open circles are used to denote radiation originating from a previous step in the sequence, or in the case of (b) and (e) in the longwave, thermal emission. The symbols F, G, H, I, H', and I' refer to how the different components of the flux are denoted in section 3.

clouds increases the surface longwave cloud forcing by as much as 30%. Gounou and Hogan (2007) reported that 3D transport typically increases the TOA longwave forcing of contrails by around 10%. There is a large degree of cancellation between the shortwave and longwave CRFs of contrails (Stuber et al. 2006), and therefore it turns out that the modest effects of 3D transport in the shortwave and longwave individually add up to very substantial effect on net CRF, leading to a doubling or a reversal of the sign depending on solar zenith angle (Gounou and Hogan 2007). It should be noted that the mechanism in Fig. 1c can also modulate the fraction of reflected shortwave radiation from the surface that escapes to space, but the other two mechanisms appear to dominate in the shortwave.

The results reviewed in this section so far have been for clouds with a large area of cloud side relative to their cloud cover, particularly convective clouds such as cumulus. For stratiform clouds the 3D effect is smaller because of the reduced area of cloud side. For example, Zuidema and Evans (1998) reported only around a 2% effect for the interaction of shortwave radiation with stratocumulus clouds. Zhong et al. (2008) found that optically thin cirrus had up to a 15% effect in the shortwave and 10% in the longwave, but reducing for optically thicker ice clouds.

3. Method

Figures 3a–c present a schematic of the three steps in a standard 1D radiation scheme. Figures 3d–i present the equivalent steps in our new scheme that incorporates the effects of 3D transport, which involves modifications to the three existing steps and three additional steps. Although this schematic shows cloud in only a single layer, the new method is designed to be applied with the multilayer representation of the atmosphere used in GCMs, with clouds in an arbitrary number of the layers. Thus, the shadowing of one cloud by another is treated by standard cloud overlap methods that define the degree of overlap at layer edges.

These procedures represented in Fig. 3 are described in full in the following subsections. Section 3a describes how the treatment of the direct incoming shortwave beam may be modified to include radiation exchange between regions. In the shortwave, scattering from the direct beam then acts as a source for the calculation of the diffuse radiation field, while in the longwave, the source for the diffuse radiation field is thermal emission. Section 3b describes how the distribution of sources with height in a single atmospheric layer can be used to calculate the exitant fluxes at the top and bottom of the layer; transport through cloud sides is represented via a two-stage process illustrated by Figs. 3e,f. Finally, section 3c describes how the sources at layer edges, together with the reflectance and transmittance of each layer, may be used with a discretized version of the two-stream equations to calculate the vertical distribution of upwelling and downwelling diffuse fluxes in the atmosphere. Again, to represent transport through cloud sides, a three-stage process is employed as illustrated in Figs. 3g–i.

The equations presented in this section are all monochromatic in the sense that they are valid over a part of the spectrum narrow enough that the scattering and absorption properties of the atmosphere can be considered constant. For simplicity, however, the dependence of each term on wavelength has not been written.

a. Direct solar beam

The first step of a 1D radiation calculation in the shortwave part of the spectrum is to determine how much of the direct (i.e., unscattered) beam penetrates down to any point in the atmosphere. In the case where the atmosphere is divided into discrete layers, we have to solve

$$\frac{dF}{dz} = -\frac{\beta_e}{\mu_0} F \tag{2}$$

in each layer, where $F(z)$ is the direct solar irradiance at a particular point in the layer, z is physical depth from the top of the layer down to that point, μ_0 is the cosine of the solar zenith angle, and β_e is the volume extinction coefficient. The solution of (2) is Beer's law, given by

$$F(z) = F_0 \exp\left(-\frac{\beta_e z}{\mu_0}\right), \tag{3}$$

where F_0 is the incoming solar irradiance into a plane that is parallel to the surface of the earth at the wavelength under consideration. In each layer, Beer's law is applied separately to each region within it and, if there are multiple regions in each layer (e.g., clear and cloudy), overlap rules are used to determine how the exitant irradiances at the base of that layer are combined to obtain the input irradiances at the top of the regions of the next layer. At the surface, a Lambertian reflector would be represented by treating all of the direct beam that is reflected by the surface as a boundary source term for the diffuse radiation calculation using the two-stream equations (see section 3c). Note that the optical depth and other single-scattering properties refer to delta-Eddington-scaled quantities (Joseph et al. 1976).

So how can we account for the direct beam of the sun passing through the sides of clouds? We need to modify (2) for each region to account for lateral exchange of radiation between regions. We use the same approach as Malvagi et al. (1993): add two extra terms to (2)—one to account for loss of radiation from the region, the other to account for gain of radiation from the other region. Since the optical depth of each region will be different, it is necessary to define a common vertical coordinate. We use height coordinate z that increases with depth downward into the layer from zero at the top to z_1 at the base.

Thus, for two regions a and b, we require the corresponding irradiances $F^a(z)$ and $F^b(z)$ to satisfy

$$\frac{dF^a}{dz} = -\frac{\beta_e^a}{\mu_0} F^a - f_{\text{dir}}^{ab} F^a + f_{\text{dir}}^{ba} F^b,$$

$$\frac{dF^b}{dz} = -\frac{\beta_e^b}{\mu_0} F^b - f_{\text{dir}}^{ba} F^b + f_{\text{dir}}^{ab} F^a, \tag{4}$$

where β_e^a and β_e^b are the volume extinction coefficients of the two regions of the layer, f_{dir}^{ab} represents the rate at which radiation is laterally transported from region a to region b, and conversely for f_{dir}^{ba}.

To avoid breaking the flow of the discussion, we postpone the description of the derivation of these rates until section 4. It is important to define F^a and F^b (which have units of watts per square meter) as the radiative power in a particular region divided by the area of the entire grid box (all regions). This ensures that energy is conserved when the same rate $f_{\text{dir}}^{ab} F^a$ is used for the power leaving region a as the power entering region b. It also means that the mean irradiance of the entire grid box is simply $F = F^a + F^b$. In writing (4) we are assuming that, at any height in the layer, the radiation in a particular region is evenly distributed across it, so that the rate of escape to another region is simply proportional to the mean irradiance in the region.

Equation 4 may be solved as a pair of coupled ordinary differential equations (ODEs) assuming that the incoming irradiances at the top of the layer, $F^a(0)$ and $F^b(0)$, are known. The solution is

$$F^a(z) = \frac{(q + a - b)F^a(0) - 2f_{\text{dir}}^{ba}F^b(0)}{2q} \exp(k_1 z)$$

$$+ \frac{(q - a + b)F^a(0) + 2f_{\text{dir}}^{ba}F^b(0)}{2q} \exp(k_2 z),$$

$$F^b(z) = \frac{(q - a + b)F^b(0) - 2f_{\text{dir}}^{ab}F^a(0)}{2q} \exp(k_1 z)$$

$$+ \frac{(q + a - b)F^b(0) + 2f_{\text{dir}}^{ab}F^a(0)}{2q} \exp(k_2 z), \tag{5}$$

where

$$a = \beta_e^a/\mu_0 + f_{\text{dir}}^{ab}, \tag{6}$$

$$b = \beta_e^b/\mu_0 + f_{\text{dir}}^{ba}, \tag{7}$$

$$q = (a^2 + b^2 - 2ab + 4f_{\text{dir}}^{ab}f_{\text{dir}}^{ba})^{1/2}, \tag{8}$$

$$k_1 = -(a + b + q)/2, \quad \text{and} \tag{9}$$
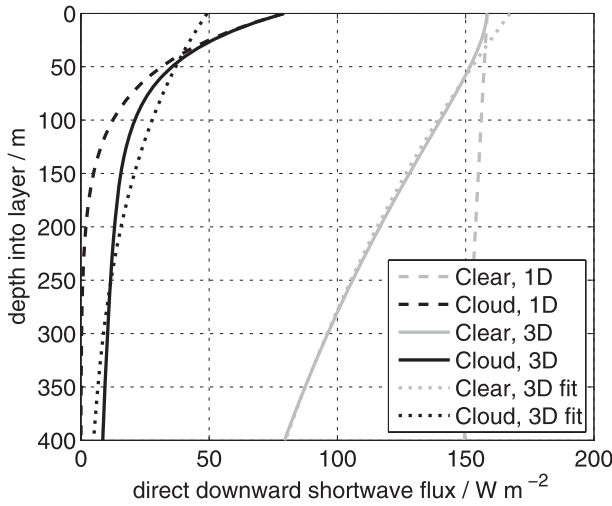
$$k_2 = -(a + b - q)/2. \tag{10}$$

FIG. 4. Simulation of the effect of lateral transport on the direct downwelling shortwave irradiance F in a layer vs the depth into the layer z. The layer contains two regions: a cloud with cloud fraction $1/3$, optical depth 5 (before delta-Eddington scaling), asymmetry factor 0.85, and vertical-to-horizontal aspect ratio unity, and a clear-sky region with an optical depth of 0.01. The solar zenith angle is 80°, and the irradiances entering the top of the clear and cloudy regions are in proportion to their areal coverage. The dashed lines show the profiles for the clear and cloudy regions in the independent column approximation, each obeying Beer's law. The solid lines show the same but with lateral transport modeled by (5). The dotted line shows the single-exponential fit to the two-exponential solution, required in section 3b.

It can be shown by substitution that in the case of zero lateral transport between regions ($f_{\text{dir}}^{ab} = f_{\text{dir}}^{ba} = 0$), the solutions given by (5) reduce to Beer's law for the two regions separately.

Figure 4 compares the profile of direct fluxes in clear and cloudy regions for a case with a cloud cover of $1/3$ and a solar zenith angle of 80°. The dashed lines correspond to a standard 1D radiation scheme in which transport between regions is neglected and it can be seen that almost all of the radiation incident at the top of the clear-sky region reaches the bottom, while virtually none reaches the bottom of the cloudy region. In contrast, the solid lines include the effect of transport between regions described by (5). Here it can be seen that more than half of the radiation that enters the top of the clear-sky region passes through the side of the cloud before reaching the base of the clear-sky region, resulting in a nonnegligible amount of direct-beam radiation in the cloudy region at all heights.

To determine the irradiances at the base of regions a and b of the layer, we substitute $z = z_1$ into (5). As before, overlap rules are then used to determine how the irradiances are combined to find the inputs at the top of

the next layer down in the atmosphere. It can be seen in Fig. 4 that there is a considerable reduction of order 40% in the total direct flux reaching the base of the layer, as would be expected from the conceptual model of shortwave side illumination presented in Fig. 1a.

This may be extended to treat more than two regions, such as the Tripleclouds scheme of Shonk and Hogan (2008), where horizontally inhomogeneous clouds are treated as two internally homogeneous regions (in addition to the clear-sky region) with different optical depths. In this case, (4) would be extended to include an extra equation for the irradiance in the third region $F^c(z)$, and additional terms would be added to each of the three equations to represent the gain to or loss from region c. In this case the solution for two regions presented in (5)–(10) would be replaced by the solution for three regions.

b. Diffuse edge sources

To describe the transport of the diffuse component of the radiation field, the two-stream equations are employed. They treat the radiation into the upward and downward hemispheres as a pair of irradiances G^+ and G^- that are assumed to travel in discrete directions $+\mu_1$ and $-\mu_1$, respectively. Values for μ_1 vary between radiation schemes, but a typical value is 0.6 (Fu et al. 1997), corresponding to a zenith angle θ_1 of 53°. The first part is applied independently in each layer to work out how much of the source in the interior of the layer emerges from the top and bottom of that layer. These "edge sources" are then used in the second two-stream step described in section 3c.

In the familiar 1D case with lateral transport between regions, the two-stream equations form a pair of coupled ODEs that may be applied separately within each region of a given layer of the atmosphere. To represent 3D effects, we may apply the same procedure as for the direct beam, and add lateral transport terms, such that the two-stream equations become

$$\frac{dG^{a-}}{dz} = \beta_e^a(-\gamma_1^a G^{a-} + \gamma_2^a G^{a+} + S_F^{a-})$$
$$- f_{\text{diff}}^{ab} G^{a-} + f_{\text{diff}}^{ba} G^{b-},$$

$$-\frac{dG^{a+}}{dz} = \beta_e^a(-\gamma_1^a G^{a+} + \gamma_2^a G^{a-} + S_F^{a+})$$
$$- f_{\text{diff}}^{ab} G^{a+} + f_{\text{diff}}^{ba} G^{b+}, \qquad (11)$$

and similarly for region b. Other regions may be added by including further terms for the exchange between

them. Within the parentheses on the right-hand side, the three terms are as in the standard two-stream equations, representing respectively the loss by scattering and absorption (except for radiation that is scattered but remains within the same hemisphere), gain by scattering from the other direction, and internal sources (i.e., scattering from the direct beam in the shortwave and thermal emission in the longwave). Scattering and absorption are governed by the coefficients γ_1 and γ_2, given by

$$\gamma_1 = \frac{1}{\mu_1}\left[1 - \frac{\omega(1+g)}{2}\right] \quad \text{and} \quad (12)$$

$$\gamma_2 = \frac{1}{\mu_1}\left[\frac{\omega(1-g)}{2}\right], \quad (13)$$

where ω and g are the single-scattering albedo and asymmetry factor of the medium. Note that other formulations for these terms have been proposed in the literature (Meador and Weaver 1980). The final two terms in (11) represent lateral transport between regions, governed by transfer coefficients f_{diff}^{ab} and f_{diff}^{ba}, which we define in section 4.

We now discuss the source terms $S_F^{\pm}(z)$. In the case of longwave radiation, thermal emission is isotropic and so $S_F^+ = S_F^- = B[T(z)]$, where B is the Planck function at temperature T in the wavelength interval being simulated. In the case of shortwave radiation, $S_F^{\pm}$ represents scattering from the direct solar beam. The rate of extinction of the direct beam in (4) is $(\beta_e/\mu_0)F$, a fraction ω of which is scattered rather than being absorbed. Therefore, the source terms are given by

$$S_F^+ = \frac{\omega\gamma_3}{\mu_0}F, \quad \text{and} \quad (14)$$

$$S_F^- = \frac{\omega(1-\gamma_3)}{\mu_0}F, \quad (15)$$

where γ_3 represents the fraction of scattered direct solar radiation that enters the upward hemisphere, and is given by

$$\gamma_3 = \frac{1 - 3g\mu_0\mu_1}{2}, \quad (16)$$

according to Liou (1980).

In principle, the solution obtained for the direct solar irradiances F in (5) could be converted to sources via (14) and (15) and substituted directly into (11), and similarly for region b. However, the fact that (5) describes F in terms of two exponentials means that the formal solution to this system has an excessively large number of terms. Therefore, we first fit a single exponential to the two exponentials using the technique given in the appendix, thus assuming that the source terms $S_F^{\pm}$ can be represented as varying exponentially with z as

$$S_F^{a+} = S_0^{a+}\exp(s_{a+}z), \quad (17)$$

and similarly for the other source terms. The coefficients S_0^{a+} and s_{a+} are the result of the fitting procedure. The dotted lines in Fig. 4 demonstrate the fact that this parameterization is usually a reasonable approximation. In the longwave it is common to assume that the Planck function varies exponentially within a layer (e.g., Fu et al. 1997), so (17) is also applicable in the longwave.

Thus (11) represents four coupled linear ODEs for G^{a+}, G^{a-}, G^{b+}, and G^{b-}. This is analogous to the four-stream discrete ordinate method for radiative transfer (e.g., Thomas and Stamnes 1999), except that rather than the four streams corresponding to irradiances in four different directions, our four streams correspond to irradiances in two directions and in two adjacent regions. However, we cannot simply apply an existing four-stream solution to the two-stream–two-region problem, because the latter lacks some of the symmetries of the former. For example, in a four-stream scheme, the rate at which radiation is scattered from stream 1 to stream 2 is equal to the rate at which radiation is scattered from stream 2 to stream 1. This symmetry does not apply if the two streams are in different regions and the regions are of different size (i.e., the cloud fraction is not equal to one-half), because then the rate at which radiation in the upwelling stream of the smaller region is transported into the upwelling stream of the larger region is greater than the rate of migration back into the smaller region. According to Thomas and Stamnes (1999), this symmetry breaking would result in a factor of 8 increase in computational time.

A useful consideration is that, in practice, the two regions are only weakly coupled. An individual photon may be scattered between the upwelling and downwelling hemispheres several times before exiting a layer, but it is much less likely to be exchanged laterally between regions more than once before exiting the layer through the base or the top. If we make the assumption that the diffuse radiation passes laterally through a cloud edge at most once, then the four coupled equations represented by (11) (and the equivalent equations for $G^{b\pm}$) can be replaced by two pairs of coupled equations that are solved independently in a two-step process illustrated by Figs. 3e and 3f. In principle, this assumption may be relaxed by using more than two steps, in which each subsequent step accounts for the probability of radiation passing laterally through a cloud edge one more

time, but in practice two steps are sufficient to capture the leading-order 3D effects. In the first step, the source terms in (11) representing transport from the other region are removed while the sink term that is due to lateral transport out of the region is retained, yielding

$$\frac{dG^{a-}}{dz} = \beta_e^a(-\hat{\gamma}_1^a G^{a-} + \gamma_2^a G^{a+} + S_F^{a-}),$$

$$-\frac{dG^{a+}}{dz} = \beta_e^a(-\hat{\gamma}_1^a G^{a+} + \gamma_2^a G^{a-} + S_F^{a+}), \quad (18)$$

where we have incorporated this sink into an "effective γ_1" of the form

$$\hat{\gamma}_1^a = \gamma_1^a + f_{\text{diff}}^{ab}/\beta_e^a. \quad (19)$$

A similar pair of equations may be written for region b. In this step we are treating radiation that escapes through cloud sides to be lost to the system, to be picked up only in the second step.

The equations in (18) are in the same two-stream form as considered by Thomas and Stamnes (1999) and Fu et al. (1997). Therefore, we may apply the same solution to obtain the exitant fluxes at the top and bottom of the layer that are due to the sources $S_F^{a\pm}$. Neglecting the superscript a for brevity, the solution for $G^\pm$ has the form

$$G^+(z) = g_1 t \exp(kz) + g_2 r \exp(-kz) + Z^+(z),$$

$$G^-(z) = g_1 rt \exp(kz) + g_2 \exp(-kz) + Z^-(z), \quad (20)$$

where the first two terms on the right-hand side represent the solution to the homogeneous part of (18) (i.e., with the sources set to zero), where

$$k = \beta_e(\hat{\gamma}_1^2 - \gamma_2^2)^{1/2}, \quad (21)$$

$$r = \frac{\beta_e \hat{\gamma}_1 - k}{\beta_e \gamma_2} = \frac{\beta_e \gamma_2}{\beta_e \hat{\gamma}_1 + k}, \quad \text{and} \quad (22)$$

$$t = \exp(-kz_1), \quad (23)$$

while $Z^\pm$ is the particular solution, related to the inhomogeneous part of (18) (the source terms), and is given by

$$Z^+(z) = \beta_e \left[\frac{s_+ + \beta_e \hat{\gamma}_1}{k^2 - s_+^2} S_F^+(z) + \frac{\beta_e \gamma_2}{k^2 - s_-^2} S_F^-(z) \right],$$

$$Z^-(z) = \beta_e \left[\frac{\beta_e \hat{\gamma}_1 - s_-}{k^2 - s_-^2} S_F^-(z) + \frac{\beta_e \gamma_2}{k^2 - s_+^2} S_F^+(z) \right], \quad (24)$$

and the $s_\pm$ terms describe the height distribution of the upwelling and downwelling source following (17). The coefficients g_1 and g_2 may be determined from boundary conditions—that is, by substituting zero for the downwelling irradiance at the top of the layer $G^-(0)$ and the upwelling irradiance at the base of the layer $G^+(z_1)$. This yields

$$g_1 = \frac{Z^+(z_1) - rtZ^-(0)}{r^2 t^2 - 1},$$

$$g_2 = \frac{Z^-(0) - rtZ^+(z_1)}{r^2 t^2 - 1}, \quad (25)$$

where the $Z^\pm(0)$ and $Z^\pm(z_1)$ terms are found by substituting the known source terms given by (17) into (24) at the top and bottom of the layer, respectively.

Thus, we derive the exitant irradiance at the top and base of region a and layer i, due solely to the sources within that region, as

$$\Sigma_G^{a+} = G^{a+}(0) = Z^+(0)$$

$$+ \frac{Z^+(z_1)(1 - r^2)t + Z^-(0)(1 - t^2)r}{r^2 t^2 - 1},$$

$$\Sigma_G^{a-} = G^{a-}(z_1) = Z^-(z_1)$$

$$+ \frac{Z^+(z_1)(1 - t^2)r + Z^-(0)(1 - r^2)t}{r^2 t^2 - 1}. \quad (26)$$

We use the notation Σ for the edge sources to avoid confusion with the continuous source distribution S described previously. The arrows reaching the top of the cloudy region in Fig. 3e display schematically the component of the radiation field represented by Σ_G^{a+} above.

The extra step to represent 3D transport, depicted in Fig. 3f, is to calculate what happens to the radiation that escaped through the cloud sides. We perform a second diffuse source calculation, but this time using the radiation entering region b from region a as the source function and setting the lateral radiation transfer rates to zero, as no further lateral transfer is allowed in this second step. As the distribution of diffuse radiation through each region is different in this second step, we use the notation $H^\pm$ in place of $G^\pm$. This gives

$$\frac{dH^{a-}}{dz} = \beta_e^a(-\gamma_1^a H^{a-} + \gamma_2^a H^{a+} + S_G^{a-}),$$

$$-\frac{dH^{a+}}{dz} = \beta_e^a(-\gamma_1^a H^{a+} + \gamma_2^a H^{a-} + S_G^{a+}), \quad (27)$$

where the sources are

$$S_G^{a-}(z) = \frac{f_{\text{diff}}^{ba}}{\beta_e^a} G^{b-}(z),$$

$$S_G^{a+}(z) = \frac{f_{\text{diff}}^{ba}}{\beta_e^a} G^{b+}(z). \tag{28}$$

Similar equations can be written to account for the $S_G^{b\pm}$ sources.

Note that the form of (27) is the same as (18), but is the equivalent 1D calculation (depicted in Fig. 3b). The difference is the application of γ_1 in place of $\hat{\gamma}_1$. When (24) is substituted into (20), we find that G^{a+}, G^{a-}, G^{b+}, and G^{b-} are each represented by the sum of four exponentials. The method in the appendix is used again to approximate them by a single exponential. We can then solve (27) using exactly the same method as in the first step, but with γ_1 substituted in place of $\hat{\gamma}_1$ to give flux distributions H^{a+}, H^{a-}, H^{b+}, and H^{b-}. This gives a second set of edge sources (Σ_H^{a+}, Σ_H^{a-}, Σ_H^{b+}, and Σ_H^{b-}), which can be added respectively to the first set (Σ_G^{a+}, Σ_G^{a-}, Σ_G^{b+}, and Σ_G^{b-}) from (26) to give the total edge sources.

c. Diffuse radiation profile

The final step in the radiative transfer calculation is to use the edge sources calculated in section 3b in a multilayer implementation of the two-stream equations. The standard approach is to define reflection and transmission functions for each layer and region as follows (Meador and Weaver 1980):

$$R = \frac{\beta_e \gamma_2 (1 - t^2)}{k + \beta_e \gamma_1 + (k - \beta_e \gamma_1) t^2} \quad \text{and} \tag{29}$$

$$T = \frac{2kt}{k + \beta_e \gamma_1 + (k - \beta_e \gamma_1) t^2}, \tag{30}$$

where the terms were defined in (12)–(13) and (21)–(23). Defining the indices of the layers to increase downward, the upwelling radiative flux at the top of region a of layer i, $I_{i+1/2}^{a+}$, is the sum of transmitted flux through the layer, the fraction of the downwelling flux that is reflected back, and the upwelling source from the layer:

$$I_{i-1/2}^{a+} = T_i^a I_{i+1/2}^{a+} + R_i^a I_{i-1/2}^{a-} + \Sigma_i^{a+}, \tag{31}$$

and similarly for region b. Likewise, the downwelling flux at the base of region a of layer i is given by

$$I_{i+1/2}^{a-} = T_i^a I_{i-1/2}^{a-} + R_i^a I_{i+1/2}^{a+} + \Sigma_i^{a-}, \tag{32}$$

and similarly for region b. At the surface (midlevel $n - 1/2$), the upwelling flux is given by

$$I_{n-1/2}^{a+} = \alpha_s(I_{n-1/2}^{a-} + F_{n-1/2}^a) + (1 - \alpha_s)B(T_s), \tag{33}$$

where α_s is the surface albedo, $F_{n-1/2}^a$ is the direct downwelling solar radiation at the surface (zero in the longwave), and $B(T_s)$ is the Planck function at the surface temperature (assumed to be zero in the shortwave).

In the case of a horizontally homogeneous atmosphere, we have only one region a, and the equations for the upwelling and downwelling fluxes at each layer interface may be combined into a tridiagonal system of linear equations that is efficiently solved. When each layer of the atmosphere is divided into two or more regions, with arbitrary overlap between regions in different layers, the system becomes more complicated to solve. It was shown by Shonk and Hogan (2008) that the most obvious approach of writing the equations out as a linear system of equations and solving the matrix problem results in anomalous horizontal radiation transport below cloud base from the sunlit to the shadowed part of the grid box. This is clearly a serious drawback when we are trying to devise a method to calculate horizontal transport accurately. Shonk and Hogan (2008) presented an efficient method to solve the system of equations that overcomes this problem, which we use as a basis for the extension to include 3D transport.

So how may we modify (31) and (32) to include transport between regions? One approach would be to add extra terms representing gain from and loss to the adjacent region, although this turns out to be excessively complicated, and impossible to incorporate within the Shonk and Hogan (2008) solver. Instead we take a similar approach to section 3b, and assume that in the lifetime of a photon as treated by the multilayer two-stream equations, it never travels through more than one cloud side. This enables the diffuse calculation to be split into two parts. In the first part, illustrated by Fig. 3g, we use the Shonk and Hogan (2008) solver, but with an additional sink of radiation representing loss of radiation through cloud sides. This is achieved by using $\hat{\gamma}_1$ as defined in (19) in place of γ_1 in (29) and (30) to calculate modified reflection and transmission functions, $\hat{R}$ and $\hat{T}$. Applying $\hat{R}$ and $\hat{T}$ to the multilayer two-stream equations allows the calculation of the profile of upwelling and downwelling fluxes $I^{a\pm}$ and $I^{b\pm}$ due to radiation that has not passed through the side of a cloud (at least, not since its first interception of a layer boundary as discussed in section 3b). The edge source terms in (31) and (32) are defined to be the sum of the edge sources output from the previous two steps; that is, $\Sigma^{a\pm} = \Sigma_G^{a\pm} + \Sigma_H^{a\pm}$.

In the second part, we account for the laterally transported radiation that was lost to the system in the computation of the $I^{a\pm}$ and $I^{b\pm}$ profiles. This is done by computing the profile of radiation that was lost and using it as the

source function in two-step computation to find out where it goes. The first step is to compute how much reaches a layer edge and is depicted in Fig. 3h. This procedure is identical to the previous edge-source calculation depicted in Fig. 3f and described toward the end of section 3b. The second step uses the resulting edge sources as input to a multilayer two-stream calculation depicted in Fig. 3i. This procedure is the same as that depicted in Fig. 3g. Note that in neither of these two steps is further lateral transport between regions permitted.

We now describe the second part mathematically. The profiles of $I^{a\pm}$ and $I^{b\pm}$ interior to a single layer may be described as the sum of two exponentials:

$$I^{a+}(z) = A^{a+} \exp(k^{a+} z) + B^{a+} \exp(-k^{a+} z),$$
$$I^{a-}(z) = A^{a-} \exp(k^{a-} z) + B^{a-} \exp(-k^{a-} z), \qquad (34)$$

where $k^{a\pm}$ is as defined in (21) and as before z is the depth down into the layer from its top boundary. Similar equations can be written for region b. The coefficients A and B are determined from the boundary conditions, which are the fluxes at the layer boundaries obtained by solving the system of equations represented by (31) and (32). However, the presence of internal sources at layer boundaries in (31) and (32) means that $I^{a\pm}$ and $I^{b\pm}$ are actually discontinuous at layer boundaries and the boundary conditions we need to apply are

$$\begin{aligned} I^{a+}(0) &= I^{a+}_{i-1/2} - \Sigma^{a+}, \\ I^{a+}(z_1) &= I^{a+}_{i+1/2}, \\ I^{a-}(0) &= I^{a-}_{i-1/2}, \\ I^{a-}(z_1) &= I^{a-}_{i+1/2} - \Sigma^{a-}. \end{aligned} \qquad (35)$$

The variable $I^{a\pm}(z)$ describes the diffuse flux within a layer that originated from other layers, while $G^{a\pm} + H^{a\pm}$ describes the diffuse flux within a layer that originated from within the same layer (either by scattering from the direct beam or thermal emission). It is only the sum of the two that is continuous across layer boundaries. Since lateral transport has already been treated for the latter, it is only the lateral transport of the former that we need consider now.

The radiation that is lost to $I^{a\pm}$ by lateral transport is denoted $H'^{a\pm}$, and within a layer obeys the single-layer two-stream equations:

$$\frac{dH'^{a-}}{dz} = \beta_e^a(-\gamma_1^a H'^{a-} + \gamma_2^a H'^{a+} + S_I^{a-}),$$

$$-\frac{dH'^{a+}}{dz} = \beta_e^a(-\gamma_1^a H'^{a+} + \gamma_2^a H'^{a-} + S_I^{a+}), \quad (36)$$

where the source terms $S_I^{a\pm}$ represent transport from the other region and are given by

$$S_I^{a-}(z) = \frac{f_{\text{diff}}^{ba}}{\beta_e^a} I^{b-}(z) \quad \text{and} \qquad (37)$$

$$S_I^{a+}(z) = \frac{f_{\text{diff}}^{ba}}{\beta_e^a} I^{b+}(z). \qquad (38)$$

Clearly this has the same mathematical form as (27) and (28), and so we may follow the procedure in the second step of section 3b to calculate a new set of boundary sources $\Sigma_{H'}^{\pm}$ in regions a and b (depicted in Fig. 3h). These are then used as the sources in a second call of the Shonk and Hogan (2008) solver, except that this time, R and T are calculated exactly as in (29) and (30), thereby permitting no further transport between cloud sides. This generates a second profile of upwelling and downwelling fluxes $I'^{a\pm}$ (depicted in Fig. 3i), which can then be added to the first profile $I^{a\pm}$ to obtain the full set of diffuse fluxes including 3D radiative transfer. (Note that since here we are using the values of $I^{a\pm}$ and $I'^{a\pm}$ only at layer boundaries we do not need to worry about fact that these variables may be strictly discontinuous interior to individual layers, as discussed above.) In the shortwave, the direct incoming beam versus height would be added to the downwelling diffuse component to obtain the total downwelling flux profile.

4. Lateral radiation transfer rates

The lateral exchange of direct radiation between regions in a given layer is governed by coefficients f_{dir}^{ab} and f_{dir}^{ba} in (4), while the exchange of diffuse radiation is governed by f_{diff}^{ab} and f_{diff}^{ba} in (11). In this section, we derive expressions for these coefficients. To achieve this, we assume that the clouds are vertically uniform within a model level, and hence that the cloud edges are perfectly vertical surfaces. The extent to which this is a valid assumption was explored by Brooks et al. (2005).

a. Direct radiation: General considerations

We first estimate the rate at which direct radiation from the sun with solar zenith angle θ_0 will enter through the side of a cloud. Consider an infinitesimally thin layer of depth dz within a grid box that has a horizontal area of A. The grid box contains a clear-sky region of area A_a and a cloudy region of area A_b such that $A = A_a + A_b$. Figure 5a shows a plan view of the distribution of cloud in the grid box, where the area dA indicates the region of clear sky where sunlight entering at the top of dz (with the sun to the right of the scene in this case) would enter the cloud edge before reaching the bottom of this layer.
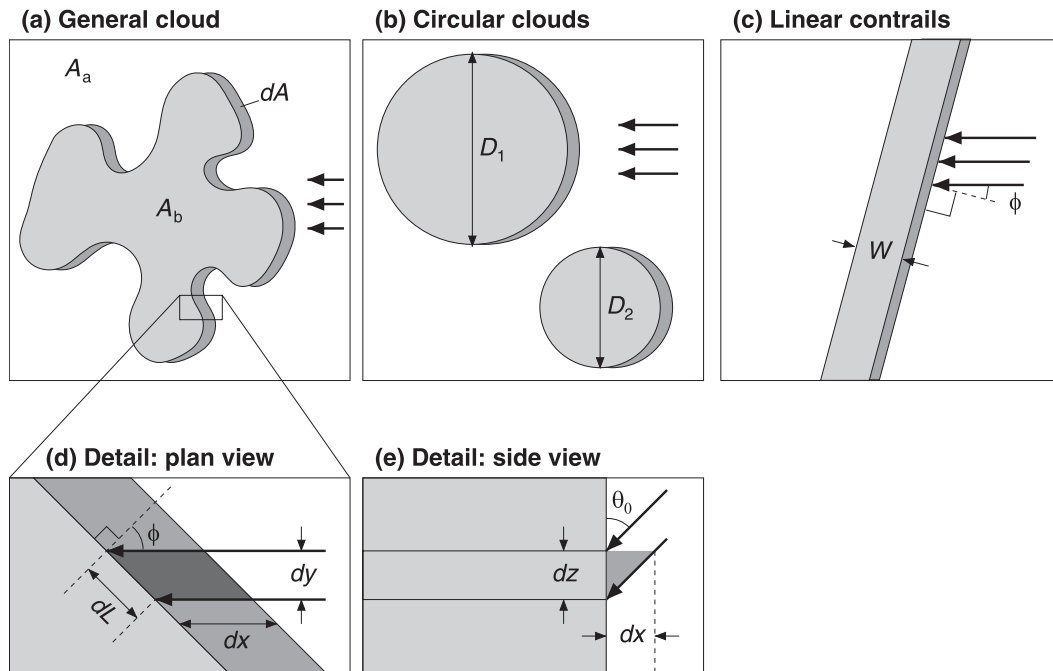
FIG. 5. Schematic illustrating how the rate at which direct-beam solar radiation enters the sides of clouds is calculated. (a) A plan view of a general cloud field in which there is no preferred orientation of the cloud edge with respect to the sun. The area dA indicates where solar radiation (from above and to the right as indicated by the thick arrows) incident on a thin layer of thickness dz would enter the cloud from the side. (b),(c) Particular cloud distributions—one with circular clouds and the other with a linear contrail. (d),(e) Magnified views of the cloud edge from above and the side, respectively, from which dA may be calculated.

As we assume incident radiation into the top of the layer to be uniformly distributed over each separate region, the change in direct flux in region a due to lateral transport to region b, dF^a, is governed by

$$\frac{dF^a}{F^a} = -\frac{dA}{A_a}. \tag{39}$$

The negative sign is because F^a is reduced with increasing depth into the layer by this transport. To calculate dA we consider the geometry of what happens at the cloud edge, depicted in plan and side views in Figs. 5d and 5e. From Fig. 5d, we can see that dA may be given by

$$dA = dx \int_L dy, \tag{40}$$

where dx is the width of infinitesimal area dA in the direction of the sun, and from Fig. 5e we have $dx = \tan(\theta_0)dz$. The integration is performed over the entire length of cloud edge L in the grid box, and dy is the length projected toward the sun by a small piece of cloud edge of length dL. From Fig. 5d we see that $dy = H(\pi/2 - |\phi|)\cos(\phi)dL$, where ϕ is the angle that the normal to the cloud edge makes to the sun. Here, $H(x)$ is the Heaviside

function (equal to 1 for $x > 0$ and 0 otherwise) and ensures that we only consider cloud edges that are sunlit— that is, those for which $|\phi| < \pi/2$. The integral will depend on the particular cloud geometry in question and will shortly be evaluated for particular cloud configurations, but we expect that, on average, the length of cloud edge for a given type of scene will increase in proportion to the gridbox area. Therefore it makes sense to define the length of cloud edge projected toward the sun per unit area as a resolution-independent property of any cloud distribution, given by

$$L_{\mathrm{dir}}^{ab} = \frac{1}{A}\int_L dy$$

$$= \frac{1}{A}\int_L H(\pi/2 - |\phi|)\cos(\phi)\,dL$$

$$= \frac{L}{A}\int_{-\pi}^{\pi} p(\phi)H(\pi/2 - |\phi|)\cos(\phi)\,d\phi. \tag{41}$$

The final form in (41) replaces the integration along the total length of cloud edge in the gridbox L with an integration over ϕ, where $p(\phi)$ is the probability density of ϕ. Substitution of (39) and (40) into the first form of (41) and rearranging gives

$$-\frac{1}{F^a}\frac{dF^a}{dz}\bigg|_{ab} = \frac{AL_{\text{dir}}^{ab}\tan(\theta_0)}{A_a}, \qquad (42)$$

where we have clarified that the derivative is only the part of the total derivative that is due to loss by transport from region a to region b. It can be seen from (4) that the left-hand side of (42) is simply the definition f_{dir}^{ab}. By defining the clear-sky fraction as $c_a = A_a/A$, we obtain

$$f_{\text{dir}}^{ab} = L_{\text{dir}}^{ab}\tan(\theta_0)/c_a. \qquad (43)$$

The same procedure may be used to derive the rate of transport between regions b and a as $f_{\text{dir}}^{ba} = L_{\text{dir}}^{ba}\tan(\theta_0)/c_b$, but on average for plausible cloud fields the length of cloud edge orientated toward the sun is equal to the length of cloud edge orientated away from the sun (the latter being associated with direct radiation escaping from region b to region a), so we have the result that $L_{\text{dir}}^{ba} = L_{\text{dir}}^{ab}$.

b. Direct radiation: Specific cases

We now have the task of defining L_{dir}^{ab} for particular cloud types and geometries. We first consider the situation in most natural cloud fields where there is no preferred orientation of the sun with respect to the cloud edge, which means that ϕ in Fig. 5d is uniformly distributed between $-\pi$ and $+\pi$; that is, $p(\phi) = 1/(2\pi)$ in (41). Hence, (41) becomes

$$L_{\text{dir}}^{ab} = \frac{L}{2\pi A}\int_{-\pi/2}^{\pi/2}\cos(\phi)\,d\phi = \frac{L}{\pi A}. \qquad (44)$$

If we have a particular 3D cloud field for which we wish to perform a radiation calculation including 3D transport using the technique developed in this paper, then it is straightforward to compute L at each height and, hence, L_{dir}^{ab} and f_{dir}^{ab}.

In a general circulation model, however, L will need to be parameterized. It is convenient to consider the idealized case of cumulus-like clouds with a circular cross section as illustrated in Fig. 5b. If a grid box contains n clouds of mean diameter $\overline{D}$ then the length of cloud edge projected toward the sun per unit area is $L_{\text{dir}}^{ab} = n\overline{D}/A$ while the cloud fraction is $c_b = (1/A)\sum_i^n \pi(D_i/2)^2 = n\pi\overline{D^2}/(4A)$. Eliminating n/A, we obtain

$$L_{\text{dir}}^{ab} = \frac{4}{\pi}\frac{c_b}{D_{\text{eff}}}, \qquad (45)$$

where the "effective cloud diameter" is $D_{\text{eff}} = \overline{D^2}/\overline{D}$. Combining (44) and (45) we obtain $D_{\text{eff}} = 4c_bA/L$, which indicates that D_{eff} may be derived as a convenient length scale from any cloud field without imposing the

assumption of circular clouds. In fact, this is exactly the same definition of effective cloud diameter considered by Jensen et al. (2008) in their analysis of satellite data, so statistics on the values of D_{eff} are already available for different cloud fields. A similar quantity has also been derived from cloud-resolving models (Neggers et al. 2003). Some convection schemes (e.g., Bechtold et al. 2001) make an explicit assumption about updraft diameter, although evaluation against observations would be needed to test whether this is sufficiently similar to the cloud diameter to be used in the radiation scheme.

Linear contrails constitute another specific cloud configuration to be considered; Fig. 5c depicts a contrail with width W whose normal makes an angle ϕ with the sun. If a model grid box contains a length X of contrail then the cloud fraction will be $c_b = XW/A$ and the total length of cloud edge will be $L = 2X$. In this case, the integral in (41) simplifies to $(\frac{1}{2})\cos(\phi)$ (where now ϕ is the angle that the normal to the contrail makes to the sun) and

$$L_{\text{dir}}^{ab} = \frac{2X}{A}\frac{\cos(\phi)}{2} = \frac{c_b\cos(\phi)}{W}. \qquad (46)$$

c. Diffuse radiation

The lateral transfer rates of diffuse radiation f_{diff}^{ab} and f_{diff}^{ba} can be calculated using the same method as for direct radiation. The differences are that in a typical two-stream scheme the radiation is assumed to be traveling with a fixed zenith angle of $\pm\theta_1$ (e.g., $\theta_1 = 53°$; Fu et al. 1997) and that the radiation is no longer entering the cloud from a single azimuth angle, but from all azimuthal directions. As a result, the equivalent of (43) for the diffuse case is

$$f_{\text{diff}}^{ab} = L_{\text{diff}}^{ab}\tan(\theta_1)/c_a, \qquad (47)$$

where L_{diff}^{ab} is the length of cloud edge projected toward the diffuse radiation field. We may use (41) but redefine ϕ as the angle between the normal to the cloud edge and the direction of incidence of a particular ray of light. Since diffuse radiation by definition has a random azimuthal orientation, ϕ will be uniformly distributed even if the cloud field has a preferred orientation with respect to some fixed coordinate system. This is mathematically equivalent to the case of direct radiation incident on a cloud edge with no preferred orientation described by (44), and so we have

$$L_{\text{diff}}^{ab} = L/\pi A, \qquad (48)$$

and in the case where the cloud edges are randomly orientated with respect to the sun we have $L_{\text{diff}}^{ab} = L_{\text{dir}}^{ab}$. In

TABLE 1. Values of cloud fraction c_b, vertical-to-horizontal aspect ratio r, optical depth δ, and single-scatter albedo ω from the studies simulated in Figs. 2 and 6.

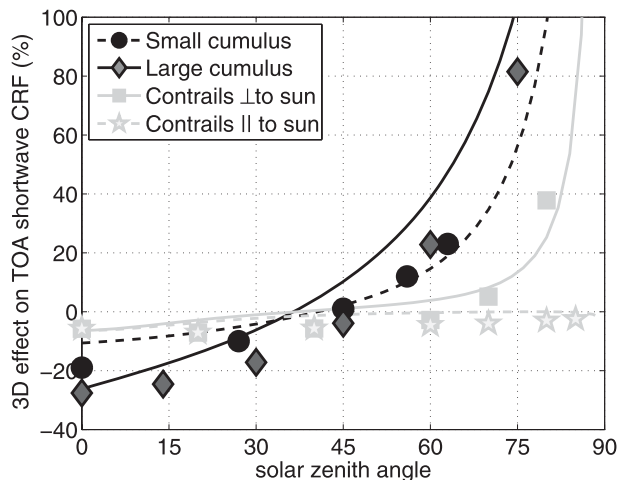| Reference	Cloud type	c_b	r	δ	ω
Benner and Evans (2001)	Small cumulus	0.10	0.4	4.4	0.999
Pincus et al. (2005)	Large cumulus	0.22	0.7	15	0.999
Gounou and Hogan (2007)	Contrails perpendicular to sun	0.05	0.5	0.4	0.999
Gounou and Hogan (2007)	Contrails parallel to sun	0.05	0.5	0.4	0.999

FIG. 6. The effect of 3D radiative transfer on shortwave TOA CRF vs solar zenith angle for cumulus clouds and contrails. The symbols are as in Fig. 2 and show the results from full 3D calculations in the literature. The lines are calculations using our modified two-stream scheme with cloud properties as close as possible to the corresponding simulations from the literature, as outlined in Table 1.

the case of linear contrails we had (46) for L_{dir}^{ab}, but to obtain the diffuse version we substitute $L = 2X$ into (48) to get

$$L_{\text{diff}}^{ab} = \frac{2X}{\pi A} = \frac{2c_b}{\pi W}. \tag{49}$$

The fact that the radiation has no preferred direction also means that the efficiency with which radiation travels from a to b is the same as from b to a, and so $L_{\text{diff}}^{ba} = L_{\text{diff}}^{ab}$.

5. Results

A simple radiation code has been created that calculates both direct and diffuse shortwave transfer based on the equations of section 3 by following the steps in Fig. 3. It performs calculations using a single shortwave wavelength band with spectrally averaged optical properties and includes both 1D and 3D versions. In this section, the ''3D effect'' computed by the new scheme (i.e., the difference in fluxes between the 3D and 1D versions) is compared to the results of full 3D radiation calculations reported in the literature. We then further investigate the behavior of the new scheme by computing the full flux profiles at two solar zenith angles. As will be shown, this is sufficient to demonstrate the potential of the technique, so we leave it to a future paper to apply this scheme in a full radiation code incorporating spectral bands.

We begin by performing simulations of the full radiative transfer calculations reported in the studies in Table 1. We use a three-layer domain with the cloud contained in the middle layer; the top and bottom layers of the domain are cloud free. All clear-sky regions have an optical depth of 0.01, an asymmetry factor of 10^{-5}, and single-scatter albedo of 0.999 99. The physical depth of the cloud-free layers does not enter the calculation; the cloudy layer has a physical depth of $z_1 = 400$ m. The cloud fractions and optical properties allotted to the

cloudy region in the middle layer are taken from the values reported in the studies, again listed in Table 1. For the cumulus cases, we take the clouds to be circular. The effective cloud diameter can be expressed in terms of aspect ratio r via

$$r = \frac{z_1}{D_{\text{eff}}}. \tag{50}$$

Combining this equation with (45) yields equations for L_{dir}^{ab} and L_{diff}^{ab}. For linear contrails, we can express the contrail width in terms of aspect ratio using

$$r = \frac{z_1}{W}. \tag{51}$$

Similarly, this can be combined with (46) and (49) to determine L_{dir}^{ab} and L_{diff}^{ab}. The coefficients f_{dir}^{ab}, f_{dir}^{ba}, f_{diff}^{ab}, and f_{diff}^{ba} can then be found using (43) and (47). For each case, we perform three radiative transfer calculations: one using our new 3D method, one performing a traditional 1D two-stream calculation, and a clear-sky calculation to enable CRF to be determined and, hence, the percentage shift to be found as in Fig. 2.

The CRF for the 1D and 3D are compared with the reported values in Fig. 6. The markers in this figure are exactly the same as in Fig. 2, indicating the percentage effects on CRF of introducing 3D transport; the lines now show the CRF effects calculated using our code over all solar zenith angles. The general features are the same and, in all cases, the compensating effects of
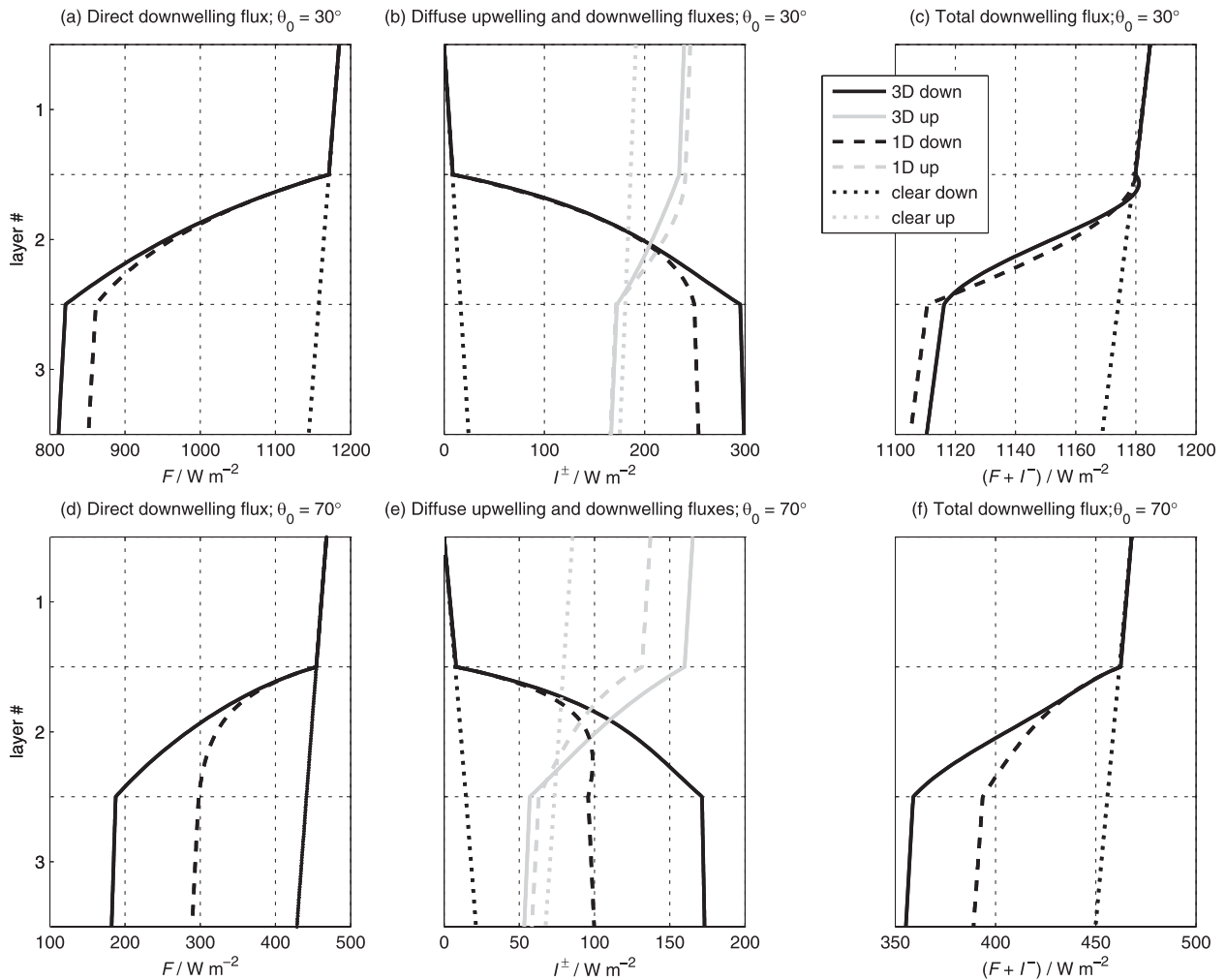
FIG. 7. Domain-mean (i.e., clear sky plus cloudy) profiles of upward and downward direct and diffuse fluxes from the 1D and 3D components of our simple radiation code. The fluxes are for a three-layer model, with cloud situated in the central layer; the properties of the cloud are the same as the large cumulus case in Table 1. (a),(d) Comparison of the direct flux profiles. (b),(e) Comparison of the upward and downward diffuse flux profiles. (c),(f) Comparison of the sum of the direct and downward diffuse fluxes. All panels also contain a profile of clear-sky flux for calculation of cloud radiative forcing.

shortwave side illumination and shortwave side escape can be clearly identified. For both types of cumulus cloud and the perpendicular contrails, at high solar zenith angles, inclusion of 3D effects reduces the CRF magnitude, which is consistent with the description of shortwave side escape in section 2. Conversely, for higher solar zenith angles, the shift is of opposite sign, with the inclusion of 3D effects increasing the magnitude of the CRF, agreeing with the sign of the change brought about by shortwave edge escape.

In comparison with the literature values on Fig. 2, we see that, while agreement is not exact, the trends in 3D CRF shift with solar zenith angle are the same. It is perhaps unrealistic to expect exact agreement between full 3D calculations and those made by our simple, one-band

code. However, it is promising that the behavior of the CRF shift with solar zenith angle is similar, with the switch of sign between high and low solar zenith angles. It should also be borne in mind that there is currently no representation of subgrid cloud inhomogeneity, as we have yet to incorporate Tripleclouds (Shonk and Hogan 2008) in our two-stream scheme.

Figure 7 shows the profile of fluxes through each of the three layers for the "large cumulus" case described by the parameters in Table 1. Again, the cloud is situated in the middle layer, with clear-sky layers above and below. The properties of the clear sky are the same as above. Figures 7a–c show the fluxes for high sun ($\theta_0 = 30°$), while Figures 7d–f show the same for low sun ($\theta_0 = 70°$). For each layer, we extract the exponential coefficients

describing the distribution of downward direct, downward diffuse, and upward diffuse flux within that layer, allowing us to reproduce and compare the profiles of fluxes through the clear and cloudy layers exactly as they appear in the 1D and 3D two-stream calculations. Within the cloudy layers, the flux profiles depicted are the sum of fluxes in the clear-sky and cloudy regions. The panels show the ''3D effect'' on profiles of direct (Figs. 7a,d), upward and downward diffuse (Figs. 7b,e), and total downward (Figs. 7c,f) fluxes when lateral transport is permitted.

The effect of shortwave side illumination is clearly evident in Figs. 7a,d. When the sun is low in the sky, the direct flux through the cloudy layer is attenuated much more rapidly when 3D transfer is permitted as the direct beam is intercepted by cloud side. The effects of shortwave side escape are trickier to identify in the flux profiles, as the combined effects of both shortwave side illumination and escape affect the diffuse flux profiles. Nevertheless, consideration of the total fluxes at the surface and the top of the atmosphere at the two chosen solar zenith angles indicate that the two shortwave effects are both occurring: at $\theta_0 = 70°$, we find a 54.3% increase in top-of-atmosphere cloud radiative forcing, which switches sign to -27.1% at $\theta_0 = 30°$ as shortwave side escape becomes the dominant effect. The 3D effects on surface CRF yield similar results: the two numbers being 55.5% and -23.3%, respectively.

6. Summary and conclusions

In this paper we have described a novel method to account for the effects of 3D radiative transfer within a two-stream radiation code. First, extra terms are added to the equations describing the vertical distribution of direct radiation in each layer to represent the lateral exchange of radiation between clear and cloudy regions. These are solved to obtain a modified version of Beer's law. The effect of 3D transport on the diffuse radiation field is likewise tackled by introducing new terms into the two-stream equations, the solution of which requires several extra stages of computation as depicted graphically in Fig. 3.

To test this idea, a simple single-band radiation scheme has been implemented that can model shortwave radiative transfer through a column of partially cloudy layers. The difference between this and a traditional 1D calculation enables the fractional change to the cloud radiative forcing (CRF) due to 3D effects to be quantified. This has been compared with the results of full 3D calculations reported in the literature for cumulus clouds and aircraft contrails. Using the same cloud optical properties and cloud fraction as reported in these studies, we calculated

the ''3D effect'' for a range of solar zenith angles. It was found that, while agreement between our results and their results was not exact, the dependence on solar zenith angle was similar. At low solar zenith angles, the effect of shortwave side escape was seen to dominate, leading to a reduction in top-of-atmosphere CRF; at high solar zenith angles, the effect of shortwave side illumination was seen to dominate, leading to an increase in top-of-atmosphere CRF. For the cases we considered, the 3D effects varied from about -30% up to over $+100\%$. These results confirm the importance of the first two mechanisms we identified in Fig. 1. It should be noted that the only other fast method for 3D radiative transfer suitable for general circulation models (GCM), the EXP-SZA-RAN method of Tompkins and DiGiuseppe (2007), cannot represent the second effect, shortwave side escape, and so would not be able to reproduce the negative 3D effect at low solar zenith angles.

Our scheme for incorporating 3D transport is estimated to be around twice the computational expense of the equivalent 1D scheme. This is adequate for implementation in a GCM for research purposes but, for operational weather forecasting or climate simulation, further work may be required to improve the efficiency. A few further developments are required before the scheme would be ready for implementation in a GCM, or to be used offline on reanalysis cloud fields to estimate the global impact of 3D radiative transfer:

(i) Our method needs to be implemented within a multiband scheme for representing the spectral variation of gaseous absorption. The current lack of a spectrally varying gaseous absorption might explain the differences in Fig. 6.

(ii) It would be ideal if the new 3D capability could be combined with a scheme for representing subgrid cloud inhomogeneity. Since our method explicitly calculates the lateral flux between clear and cloudy regions, it would be applicable to the Tripleclouds method of Shonk and Hogan (2008) and to also compute the lateral flux between the optically thin and optically thick cloudy regions in each layer with a slight increase in mathematical complexity. Our 3D scheme is unfortunately not directly compatible with the Monte Carlo Independent Column Approximation (McICA) of Pincus et al. (2003), since the independence of each column enables a different spectral band to be used in each column, making lateral transport between columns impossible. Some hybrid of our 3D scheme and the ideas behind McICA and is conceivable, but considerable further work would be required.

(iii) The lateral radiation transfer needs to be extended to treat longwave radiation. This can be achieved simply by replacing the solar source term in (18) by the Planck function, which will allow the mechanism of longwave side exchange to be represented, depicted in Fig. 1c.

(iv) Finally, section 4 showed how our method requires one number in each grid box to specify the length of cloud edge projected toward the sun per unit area L_{diff}^{ab}, which for natural clouds can be assumed to be the same for direct and diffuse radiation. The challenge is then to estimate suitable values to use for this quantity within a GCM for particular cloud scenarios. As discussed in section 4, this information could be derived from observations (e.g., Jensen et al. 2008) or in some cases the model itself (e.g., Bechtold et al. 2001).

Once these developments are implemented, a more detailed evaluation of the new scheme will be possible comparing against full 3D radiation calculations in a wide variety of cumulus and other broken-cloud scenes.

APPENDIX

Approximating the Sum of Exponentials by One Exponential

In this appendix we show how a sum of n exponentials of the form

$$F(z) = \sum_{i=1}^{n} A_i \exp(a_i z) \qquad (A1)$$

may be approximated by a single exponential of the form

$$\hat{F}(z) = B \exp(bz), \qquad (A2)$$

in the range $0 \leq z \leq z_1$. This is necessary since (5) provides the vertical distribution of direct solar radiation as the sum of two exponentials, whereas in section 3b, it is required in the form of (17) [i.e., (A2)].

We specify that the single exponential should conserve both the zeroth and first moments of (A1)—that is, the total radiative energy E between $z = 0$ and $z = z_1$—and the mean photon position $\bar{z}$. The total energy is given by

$$E = \int_0^{z_1} F(z)\, dz = \sum_{i=1}^{n} A_i (e^{a_i z_1} - 1)/a_i \qquad (A3)$$

and

$$\bar{z} = \frac{1}{E} \int_0^{z_1} F(z)z\, dz = \frac{1}{E} \sum_{i=1}^{n} A_i [e^{a_i z_1}(a_i z_1 - 1) + 1]/a_i^2. \qquad (A4)$$

The energy may be conserved exactly and the mean position reproduced closely by (A2) if its coefficients are given by

$$b = \frac{\pi}{z_1}[\tan(\pi\hat{z}) - \pi(\hat{z}^3 - \hat{z}/4)] \quad \text{and} \qquad (A5)$$

$$B = Eb/(e^{bz_1} - 1), \qquad (A6)$$

where $\hat{z} = \bar{z}/z_1 - 1/2$.

REFERENCES

Barker, H. W., 1996: A parameterization for computing grid-averaged solar fluxes for inhomogeneous marine boundary layer clouds. Part I: Methodology and homogeneous biases. *J. Atmos. Sci.,* **53,** 2289–2303.

——, G. L. Stephens, and Q. Fu, 1999: The sensitivity of domain-averaged solar fluxes to assumptions about cloud geometry. *Quart. J. Roy. Meteor. Soc.,* **125,** 2127–2152.

Bechtold, P., E. Bazile, F. Guichard, P. Mascart, and E. Richard, 2001: A mass-flux convection scheme for regional and global models. *Quart. J. Roy. Meteor. Soc.,* **127,** 869–886.

Benner, T. C., and K. F. Evans, 2001: Three-dimensional solar radiative transfer in small tropical cumulus fields derived from high-resolution imagery. *J. Geophys. Res.,* **106** (D14), 14 975–14 984.

Brooks, M. E., R. J. Hogan, and A. J. Illingworth, 2005: Parameterizing the difference in cloud fraction defined by area and by volume as observed with radar and lidar. *J. Atmos. Sci.,* **62,** 2248–2260.

Cahalan, R. F., W. Ridgway, W. J. Wiscombe, S. Gollmer, and Harshvardhan, 1994: Independent pixel and Monte Carlo estimates of stratocumulus albedo. *J. Atmos. Sci.,* **51,** 3776–3790.

DiGiuseppe, F., and A. M. Tompkins, 2003: Three-dimensional radiative transfer in tropical deep convective clouds. *J. Geophys. Res.,* **108,** 4741, doi:10.1029/2003JD003392.

Evans, K. F., 1998: The spherical harmonic discrete ordinate method for three-dimensional atmospheric radiative transfer. *J. Atmos. Sci.,* **55,** 429–446.

Fu, Q., K. N. Liou, M. C. Cribb, T. P. Charlock, and A. Grossman, 1997: Multiple scattering parameterization in thermal infrared radiative transfer. *J. Atmos. Sci.,* **54,** 2799–2812.

Gounou, A., and R. J. Hogan, 2007: A sensitivity study of the effect of horizontal photon transport on the radiative forcing of contrails. *J. Atmos. Sci.,* **64,** 1706–1716.

Heidinger, A. K., and S. K. Cox, 1996: Finite-cloud effects in longwave radiative transfer. *J. Atmos. Sci.,* **53,** 953–963.

Jensen, M. P., A. M. Vogelmann, W. D. Collins, G. J. Zhang, and E. P. Luke, 2008: Investigation of regional and seasonal variations in marine boundary layer cloud properties from MODIS observations. *J. Climate,* **21,** 4955–4973.

Joseph, J. H., W. J. Wiscombe, and J. A. Weinman, 1976: The delta-Eddington approximation for radiative flux transfer. *J. Atmos. Sci.,* **33,** 2452–2459.

Killen, R. M., and R. G. Ellingson, 1994: The effect of shape and spatial distribution of cumulus clouds on longwave irradiance. *J. Atmos. Sci.,* **51,** 2123–2136.

Lane-Veron, D. E., and R. C. J. Somerville, 2004: Stochastic theory of radiative transfer through generalized cloud fields. *J. Geophys. Res.,* **109,** D18113, doi:10.1029/2004JD004524.

Liou, K.-N., 1980: *An Introduction to Atmospheric Radiation.* International Geophysics Series, Vol. 26, Academic Press, 392 pp.

Malvagi, F., R. N. Byrne, G. C. Pomraning, and R. C. J. Somerville, 1993: Stochastic radiative transfer in a partially cloudy atmosphere. *J. Atmos. Sci.,* **50,** 2146–2158.

Meador, W. E., and W. R. Weaver, 1980: Two-stream approximations to radiative transfer in planetary atmospheres: A unified description of existing methods and a new improvement. *J. Atmos. Sci.,* **37,** 630–643.

Morcrette, J., and C. Jakob, 2000: The response of the ECMWF model to changes in the cloud overlap assumption. *Mon. Wea. Rev.,* **128,** 1707–1732.

Neggers, R. A. J., A. P. Siebesma, and H. J. J. Jonker, 2003: A multi-parcel model for shallow cumulus convection. *J. Atmos. Sci.,* **60,** 1060–1074.

Oreopoulos, L., and R. F. Cahalan, 2005: Cloud inhomogeneity from MODIS. *J. Climate,* **18,** 5110–5124.

Pincus, R., H. W. Barker, and J. Morcrette, 2003: A fast, flexible, approximate technique for computing radiative transfer in inhomogeneous cloud fields. *J. Geophys. Res.,* **108,** 4376, doi:10.1029/2002JD003322.

——, C. Hannay, and K. F. Evans, 2005: The accuracy of determining three-dimensional radiative transfer effects in cumulus clouds using ground-based profiling instruments. *J. Atmos. Sci.,* **62,** 2284–2293.

——, R. Hemler, and S. A. Klein, 2006: Using stochastically generated subcolumns to represent cloud structure in a large-scale model. *Mon. Wea. Rev.,* **134,** 3644–3656.

Pomroy, H. R., and A. J. Illingworth, 2000: Ice cloud inhomogeneity: Quantifying bias in emissivity from radar observations. *Geophys. Res. Lett.,* **27,** 2101–2104.

Randall, D. A., and Coauthors, 2007: Climate models and their evaluation. *Climate Change 2007: The Physical Science Basis,* S. Solomon et al., Eds., Cambridge University Press, 589–662.

Shonk, J. K. P., and R. J. Hogan, 2008: Tripleclouds: An efficient method for representing cloud inhomogeneity in 1D radiation schemes by using three regions at each height. *J. Climate,* **21,** 2352–2370.

——, and ——, 2010: Effect of improving representation of horizontal and vertical cloud structure on the earth's global radiation budget. Part II: The global effects. *Quart. J. Roy. Meteor. Soc.,* **136,** 1205–1215.

——, ——, and J. Manners, 2012: Impact of improved representation of horizontal and vertical cloud structure in a climate model. *Climate Dyn.,* **38,** 2365–2376.

Stuber, N., P. M. Forster, G. Rädel, and K. P. Shine, 2006: The importance of the diurnal and annual cycle of air traffic for contrail radiative forcing. *Nature,* **441,** 864–867.

Thomas, G. E., and K. Stamnes, 1999: *Radiative Transfer in the Atmosphere and Ocean.* Cambridge University Press, 517 pp.

Titov, G. A., 1990: Statistical description of radiation transfer in clouds. *J. Atmos. Sci.,* **47,** 24–38.

Tompkins, A. M., and F. DiGiuseppe, 2007: Generalizing cloud overlap treatment to include solar zenith angle effects on cloud geometry. *J. Atmos. Sci.,* **64,** 2116–2125.

Várnai, T., and R. Davies, 1999: Effects of cloud heterogeneities on shortwave radiation: Comparison of cloud-top variability and internal heterogeneity. *J. Atmos. Sci.,* **56,** 4206–4224.

Zhong, W., R. J. Hogan, and J. D. Haigh, 2008: Three-dimensional radiative transfer in mid-latitude cirrus clouds. *Quart. J. Roy. Meteor. Soc.,* **134,** 199–215.

Zuidema, P., and K. F. Evans, 1998: On the validity of the independent pixel approximation for boundary layer clouds observed during ASTEX. *J. Geophys. Res.,* **103** (D6), 6059–6074.